Probing the pairing symmetry of the iron pnictides with electronic Raman scattering

G. R. Boyd,[1] T. P. Devereaux,[2,3] P. J. Hirschfeld,[1] V. Mishra,[1] and D. J. Scalapino[4]

[1]*Department of Physics, University of Florida, Gainesville, Florida 32611, USA*

[2]*SLAC National Accelerator Laboratory, Stanford Institute for Materials and Energy Sciences, 2575 Sand Hill Road, Menlo Park, California 94025, USA*

[3]*Geballe Laboratory for Advanced Materials, Stanford University, Stanford, California 94305, USA*

[4]*Department of Physics, University of California, Santa Barbara, California 93106-9530, USA*

An important issue in the study of the iron-arsenic-based superconductors is the symmetry of the superconducting gap, a problem complicated by multiple gaps on different Fermi-surface sheets. Electronic Raman scattering is a flexible bulk probe which allows one in principle to determine gap magnitudes and test for gap nodes in different regions of the Brillouin zone by employing different photon polarization states. Here we calculate the clean Raman intensity for A_{1g}, B_{1g}, and B_{2g} polarizations and discuss the peak structures and low-energy power laws which might be expected for several popular models of the superconducting gap in these systems.

I. INTRODUCTION

Since their discovery,[1] there has been a considerable effort to understand the origin and nature of superconductivity in iron-pnictide materials (for early reviews see Refs. 2–4). Initial information on the structure of the gap is often provided by power laws in the temperature dependence of thermodynamic and transport properties, which are related to the topology of the superconducting gap in its nodal regions. Nuclear magnetic-resonance (NMR) studies[5–8] showed a low-temperature T^3 spin-lattice relaxation rate typical of a gap with nodes. However, penetration depth measurements[9–15] have been fit both to exponential activated T dependence, indicative of a fully gapped state, and low-T power laws. Angle-resolved photoemission (ARPES) measurements on single crystals of 122-type materials[16–21] measured the spectral gap reporting isotropic or nearly isotropic gaps on all Fermi-surface sheets. It is possible that these differences reflect genuinely different ground states in different materials. However, the complex interplay of multiband effects, unconventional pairing, and disorder leaves open the possibility that a single ground-state symmetry exists in all the Fe pnictides and that differences in measured properties can be understood by accounting for electronic structure differences and disorder.[22,23] It is likely that a consensus will be reached only after careful measurements using various probes on the same material and systematic disorder studies.

We argue here that measurement of the electronic Raman scattering in the superconducting state can provide important information on the structure of the bulk superconducting order parameter through its sensitivity to both symmetry and gap scales. Here we discuss the Raman scattering for some simple models of the Fe-pnictide superconductors. In general the energies of the peaks in the Raman intensity are directly related to the magnitude of the gaps on the various Fermi sheets. However, whether a given Raman polarization weights a given gap strongly or weakly depends on the polarization state of the measurement via the Raman vertex $\gamma_{\mathbf{k}}$. This is particularly important for superconductors where the

gap is strongly momentum dependent and was exploited successfully in cuprate materials to help determine the d-wave symmetry in those systems.[24–27] In addition, the presence of nodes and the dimensionality of the nodal manifold may be determined by comparison to low-energy power laws in the Raman intensity in different polarization states.

In the Fe-pnictide materials, density-functional theory calculations[28,29] for the paramagnetic state have generally found a multisheeted Fermi surface consisting of concentric, nearly circular hole pockets around the Γ point (here referred to as "α sheets") and nearly circular electron pockets around the M points, or $\tilde{X}$ point in the unfolded, one-Fe zone (referred to as "β sheets"). These sheets are plotted in Fig. 1. Spin-fluctuation models of pairing[30–33] have usually found
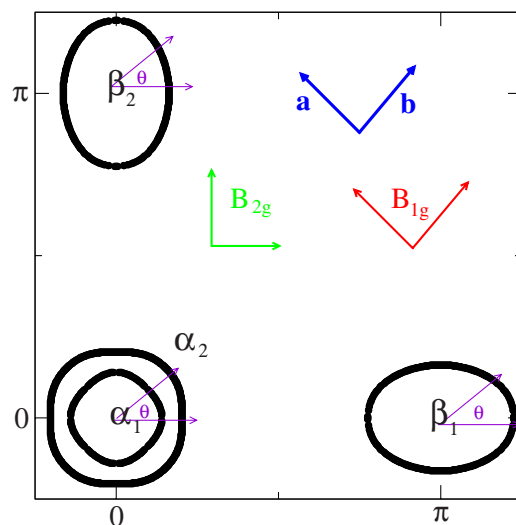

FIG. 1. (Color online) Fermi surface of model Fe pnictide represented in unfolded (one-Fe) Brillouin zone. The crystalline a,b axes are indicated in top right of the panel (blue) and the polarization geometries for incoming and scattering photon polarizations are denoted for B_{1g} and B_{2g} geometries. Note that our symmetry notation is rotated by 45° with respect to the lattice symmetries.

that the leading pairing instability had *s*-wave symmetry and noted that the next leading channel had $d_{x^2-y^2}$ symmetry. Wang *et al.*,[34] who studied the pairing problem using a functional renormalization-group approach within a five-orbital framework, also found that the leading pairing instability occurred in the *s*-wave channel and that the next leading channel had $d_{x^2-y^2}$ symmetry. These calculations differ according to whether or not actual nodes are found in the leading pairing states, but they all find large anisotropies over the Fermi-surface sheets not anticipated in the original predictions of extended-*s*-type states with isotropic gaps which changed sign between the α and β sheets.[35,36]

While ARPES experiments[16–21] have reported weakly anisotropic gaps, this may be due to momentum resolution issues and the difficulty of preparing good surfaces in these systems at present. In particular, the samples used in these experiments may be sufficiently dirty at the surface that considerable momentum averaging, with concomitant gap averaging, could be taking place.[23] Angle-dependent specific-heat measurements in a magnetic field,[37] which probe the bulk, may be feasible in the future but are difficult at present due to the requirement of large clean crystals. Raman scattering with use of different polarizations may therefore be the best current method of acquiring momentum-dependent information on the structure of the bulk superconducting order parameter. We discuss several cases below which should allow extraction of the crude momentum dependence and possible nodal structure of the order parameter over the Fermi surface. Some of these cases have been considered in an earlier paper by Chubukov *et al.*,[38] who however focused solely on the A_{1g} polarization and examined vertex corrections due to short-range interactions. However, they neglected "charge backflow" effect of the long-range part of the Coulomb interaction which is required to ensure charge conservation. Here we show that for the A_{1g} case, significant changes are to be expected due to the coupling of the A_{1g} Raman charge fluctuations due to the backflow effects.

While the expressions for the B_{1g} and B_{2g} channels are generally well characterized by the bare bubble calculation for the cuprates, it is well known that the A_{1g} contribution is significantly more complicated due to the issue of charge backflow as noted above and to the number of different excitons which may be pulled down from a gap edge condensate. In systems with several condensate pairing instabilities lying in close proximity in parameter space, strong excitonic peaks may occur. While the possibility of such excitonic modes is of interest for the pnictides, in this paper we focus on the generic quasiparticle features for Raman scattering and will consider excitonic peaks in a future publication. Charge backflow and Coulomb screening are explicitly included in all A_{1g} calculations, but pair interaction corrections will be neglected. We will however also consider the possibility that due to the form for the Raman vertices, which are allowed when there are multiple Fermi surfaces, there can also be backflow effects on symmetry channels other than A_{1g} in the Fe pnictides.

We begin in Sec. II by considering model one-band clean systems with gaps inspired by proposals for the Fe pnictides to illustrate what intuition we can gain regarding the Raman response for various polarizations. In Sec. III, we consider

gaps on all four Fermi surfaces predicted by density-functional theory. We present our conclusions in Sec. IV.

II. ELECTRONIC RAMAN SCATTERING IN CLEAN SYSTEM

A. General theory

Raman scattering is the inelastic scattering of polarized light from a material. (for a review see Ref. 24). The cross section of the scattered light is proportional to the imaginary part of the channel-dependent Raman susceptibility

$$\chi_{\gamma,\gamma}(\omega) = \int_0^\beta d\tau e^{-i\omega_m \tau} \langle T_\tau \tilde{\rho}_\gamma(\tau) \tilde{\rho}_\gamma(0) \rangle |_{i\omega_m \to w + i\delta}. \quad (1)$$

Here we will take a simple frequency independent form for the Raman vertices (nonresonant scattering) and write the effective Raman charge fluctuations in the γ channel as

$$\tilde{\rho}_\gamma = \sum_{\mathbf{k},\sigma} \sum_{n,m} \gamma_{n,m}(\mathbf{k}) c_{n,\sigma}^\dagger(\mathbf{k}) c_{m,\sigma}(\mathbf{k}), \quad (2)$$

where n, m denote band indices. $\gamma_{n,m}(\mathbf{k})$ defines the momentum- and polarization-dependent Raman vertices, which may include intra- and interband transitions. Generally, the vertex is determined by both density and current matrix elements between the conduction band and the excited states and has not been calculated for even simple metals such as Al. However, the polarization geometries of the incoming and outgoing photons impose an overall symmetry due to the way in which excitations are created in directions determined by the electric field oscillations and classifications of the anisotropy of the Raman vertices can be employed.

In this paper, in order to focus on general features for Raman scattering in the pnictides, we will neglect band structure features and treat all Fermi-surface sheets as circles. This allows for a simple symmetry classifications for the Raman vertices as has been done in the cuprates. Expanding the polarization-dependent vertices in Fermi-surface harmonics for cylindrical Fermi surfaces,

$$\gamma_n(\theta)^{A_{1g}} = a_n + b_n \cos(4\theta),$$

$$\gamma_n(\theta)^{B_{1g}} = c_n \cos(2\theta),$$

$$\gamma_n(\theta)^{B_{2g}} = d_n \sin(2\theta), \quad (3)$$

with angle-independent band prefactors a_n, b_n, c_n, d_n setting the overall strength of the Raman amplitudes for band n. Since an isotropic density fluctuation vanishes for $q \to 0$, it can be shown via Eq. (4) that the A_{1g} contribution a_n to the Raman vertex is cancelled by charge backflow and does not contribute to the scattering cross section. This leaves the $\cos(4\theta)$ as the first nonvanishing contribution in the expansion.

As shown in Fig. 1, we note that our choice of coordinates rests on the one-Fe unit cell, which is rotated by 45° with respect to the two-Fe unit cell. Thus our symmetry notation is electronic and not associated with the lattice principal di-

rections, and therefore our classifications are 45° rotated with respect to conventional lattice classifications. Using lattice coordinates, what we call B_{1g} would be B_{2g} and vice-versa. While this might create some confusion, it is convenient to understand the interplay of the angular dependence of the vertices and the energy gaps in the rotated one-Fe unit-cell frame, as shown in Fig. 1. This should be kept in mind however when one discusses, e.g., electronic excitations together with lattice excitations. Then our symmetry labels B_{1g} and B_{2g} would have to be interchanged.

Other forms for the Raman vertices are allowable, with the only requirement being that they must obey the transformation rules according to the relevant point-group symmetries of the crystal. We note that for multisheeted Fermi surfaces shown in Fig. 1, there are different possible forms for the vertices other than Eq. (9). While the Raman vertices of the α sheets must transform according to Eq. (9), for the β sheets other forms for the vertices could be admissible. This includes, for the B_{1g} vertex for example, a vertex which is momentum independent on each β sheet but of opposite sign. For the B_{2g} vertex, a Raman vertex which is p-wave-like on each β sheet (with a change of sign) would also be admissible. We will explore these possibilities in Sec. III.

For n bands crossing the Fermi level, the intraband Raman response in the absence of Coulomb screening and charge backflow is given by

$$\chi_{\tilde{\rho},\tilde{\rho}}(\omega) = \frac{1}{N}\sum_{\mathbf{k}}\sum_{n}\gamma_n(\mathbf{k})^2\lambda_n(\mathbf{k},\omega), \qquad (4)$$

where

$$\lambda_n(\mathbf{k},\omega) = \tanh\left(\frac{E_n(\mathbf{k})}{2k_BT}\right)\frac{4|\Delta_n(\mathbf{k})|^2/E_n(\mathbf{k})}{4E_n^2(\mathbf{k})-(\hbar\omega+i\delta)^2} \qquad (5)$$

is the Tsuneto function for the nth band having band dispersion $\epsilon_n(\mathbf{k})$, energy gap $\Delta_n(\mathbf{k})$, and quasiparticle energy $E_n^2(\mathbf{k})=\epsilon_n^2(\mathbf{k})+\Delta_n^2(\mathbf{k})$. Taking the imaginary part of Eq. (5) we then obtain for the Raman response at $T=0$,

$$\begin{aligned}\text{Im }\chi_{\tilde{\rho},\tilde{\rho}}(\omega) &= \sum_n \text{Im }\chi_{\tilde{\rho},\tilde{\rho}}^n(\omega) \\ &= \sum_n \frac{\pi N_{F,n}}{\omega}\text{Re}\int d\theta\gamma_n^2(\theta)\frac{|\Delta_n(\theta)|^2}{\sqrt{\omega^2-4|\Delta_n(\theta)|^2}}.\end{aligned} \qquad (6)$$

Since Raman scattering probes charge fluctuations in the long-wavelength limit, the role of the long-range Coulomb interaction is important. Isotropic charge fluctuations are coupled across all unit cells and Raman scattering at low energies must vanish due to particle number conservation, leaving only an inelastic light-scattering peak at the plasmon energy. Screening by the long-range Coulomb interaction can be taken into account by including couplings of the Raman charge density $\tilde{\rho}$ to the isotropic density ρ fluctuations and is given by

$$\chi_{\tilde{\rho},\tilde{\rho}}^{scr} = \chi_{\tilde{\rho},\tilde{\rho}} - \frac{\chi_{\tilde{\rho},\rho}\chi_{\rho,\tilde{\rho}}}{\chi_{\rho,\rho}}, \qquad (7)$$

with

$$\chi_{\tilde{\rho},\rho} = \chi_{\rho,\tilde{\rho}} = \frac{1}{N}\sum_{n}\sum_{\mathbf{k}}\gamma_n(\mathbf{k})\lambda_n(\mathbf{k}) \qquad (8)$$

and

$$\chi_{\rho,\rho} = \frac{1}{N}\sum_{n}\sum_{\mathbf{k}}\lambda_n(\mathbf{k}). \qquad (9)$$

Equations (4)–(9) constitute closed-form expressions for the intraband, nonresonant contribution to the Raman response.

It is clear that the Raman response is in general not simply additive with respect to the response calculated from each band separately. Incident photons can create anisotropic charge fluctuations according to the direction of the polarization light vector and those charge fluctuations relax by emitting a scattered photon and redistributing charge density via intrinsic electron-scattering mechanisms such as electron impurity, electron phonon, electron-electron interactions, or via breaking of Cooper pairs. The anisotropy of the charge fluctuations created with light can be controlled by aligning incident and scattered photon polarization vectors, transforming according to the elements of the irreducible point group of the crystal. For a material with D^{4h} tetragonal symmetry and a single Fermi sheet, the B_{1g} and B_{2g} Raman responses are not coupled to the long-range Coulomb interaction. As a consequence, the Raman charge densities for these channels do not couple to the pure charge-density channel and the terms given in Eq. (8) vanish. However, A_{1g} fluctuations need not vanish over the unit cell and therefore they can couple to isotropic charge density, giving the finite backflow represented by the second term in Eq. (7). We will see that this can also occur for the B_{1g} case for Raman vertices which are allowed when one has multiple Fermi surfaces as formed in the Fe pnictides.

From the expression for the Raman response we see that in the case of an isotropic gap, $\Delta_{\mathbf{k}}=\Delta$, there should always be a peak at 2Δ. In an unconventional superconductor, depending on the polarization, this absorption peak is replaced by a peak or other structure at $2\Delta_0$, twice the maximum of the gap over the Fermi surface. The peak will be rounded by scattering, but still provides a measure of the magnitude of the gaps in the system and may be compared to those determined from other experiments, e.g., ARPES and tunneling. The B_{1g} and B_{2g} vertices in Eq. (3) have zeros in $\mathbf{k}$ space and therefore weight the part of the Brillouin zone away from these zeros. This is observed, e.g., in the d-wave cuprates, where the sharp 2Δ peak occurs in the B_{1g} channel only, while a less-pronounced feature corresponding to a change in slope occurs at the same energy in the B_{2g} channel which weights the nodal regions most strongly. Furthermore, the existence of nodes in a gap creates low-energy quasiparticles that cause a nonzero response for all frequencies. This is in sharp contrast to fully gapped superconductors whose response shows a sharp gap edge with no low-energy quasiparticles. In what follows we consider separate cases of increas-

ing complexity in order to display what features for Raman scattering in a multiband system with different gap symmetries might be expected generically.

B. Results for some special cases

1. Single Fermi sheet

In order to understand the type of behavior found for the multiband models of the Fe pnictides, it is useful to begin with some special cases. Early on, motivated by the proximity of the Fe pnictides to a $(\pi,0)$ spin-density wave phase and the multiple Fermi-surface structure found in local-density approximation (LDA) calculations, a sign reversed s-wave gap was proposed.[35] It was suggested that spin-fluctuation scattering of electron pairs between the α and β Fermi sheets could lead to pairing with an isotropic s-wave gap Δ_0 that changed sign between the α and β Fermi surfaces. In this case, the Raman response would consist of a peak onsetting at $2\Delta_0$ or several peaks if there were gaps of different magnitudes on the various Fermi surfaces. In the absence of impurity scattering and inelastic lifetime effects, this peak would vary as $(\omega-2\Delta_0)^{-1/2}$ as ω approaches $2\Delta_o$ from above.

Alternatively, random-phase approximation (RPA) spin-fluctuation calculations and functional renormalization-group studies find anisotropic s-wave gaps which can even have nodes on the β Fermi surfaces as well as nearby d-wave gaps with nodes on the α Fermi surfaces. Here, in order to examine the Raman signatures of such states, we consider the simple parameterization

$$\Delta(\theta) = \frac{\Delta_0}{1+r}[1 - r\cos(2\theta)]. \tag{10}$$

This gap is plotted as a function of angle around a circular Fermi surface. Note, however, that for a single Fermi surface centered at Γ, this state would not have fourfold symmetry. Instead, the Fermi surface parameterized by θ is intended to represent a model for the β_1 sheet of the pnictides and the Fermi-surface angle θ is measured around $(\pi,0)$ rather than Γ. When combined with the β_2 sheet at $(0,\pi)$, the full s-wave symmetry of the state is restored. The gap in Eq. (10) is normalized such that Δ_0 is the maximum over the Fermi surface and plotted for the values of $r=r_\beta$ shown in Fig. 2. For $r>1$ the state has nodes on the Fermi surface and for small values of $r-1$ these nodes move toward 0 and π. For $r<1$, there are no nodes but for any nonzero r one has an anisotropic gap.

In Figs. 3 and 4 we exhibit the B_{1g}, B_{2g}, unscreened A_{1g}, and screened A_{1g} Raman responses for the gaps given by Eq. (10), which are shown in the leftmost panel in Fig. 2. In Fig. 3, where $r=1.4$, there are gap nodes on the β sheets and one finds the expected low-frequency power-law behavior in which both response functions vary as ω, following the low-energy behavior of the density of states, since the nodes of the energy gap do not align with the nodes of the Raman vertices. For the gap edge $\omega=2\Delta_{max}=2\Delta_0$, the B_{1g} and unscreened A_{1g} spectra have a $\log|\omega-2\Delta_0|$ singularity. For the B_{2g} response, there is a change of slope at $2\Delta_0$ since the
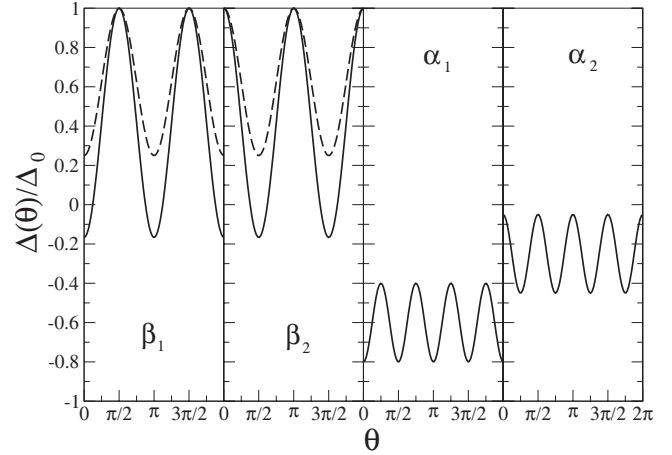

FIG. 2. The anisotropic energy gaps around the four Fermi-surface sheets as a function of angle θ shown in Fig. 1. For the β sheets, the solid line is for $r_\beta=1.4$ and the dotted line for $r_\beta=0.6$ [see Eq. (14)].

nodes of the vertex align with the gap maxima. A secondary log singularity appears at $\omega=2\Delta_{min}$, probed by the B_{1g} and A_{1g} vertices, but not B_{2g}. Screening, as pointed out before, removes all log singularities from the unscreened A_{1g} response, leaving only a cusplike behavior at $\omega=2\Delta_{min},2\Delta_{max}$.

For a nodeless anisotropic gap $(r=0.6)$ shown as the dashed line in the β_1 panel of Fig. 2, the Raman spectra are shown in Fig. 4. In this case, there is a gap in the low-frequency spectra. Here, for $r<1$, Δ_{min} occurs where the magnitude of the gap has a local minimum rather than a local maximum as it does for $r>1$. This leads to a step discontinuity at $\omega/\Delta_0=0.5$ for the B_{1g} and A_{1g} spectra rather than the log singularity seen in Fig. 3 for $r=1.6$. The nodes of the Raman vertex for the B_{2g} response are aligned with Δ_{min}, leading to a linear onset at $\omega=2\Delta_{min}$ rather than a step onset.
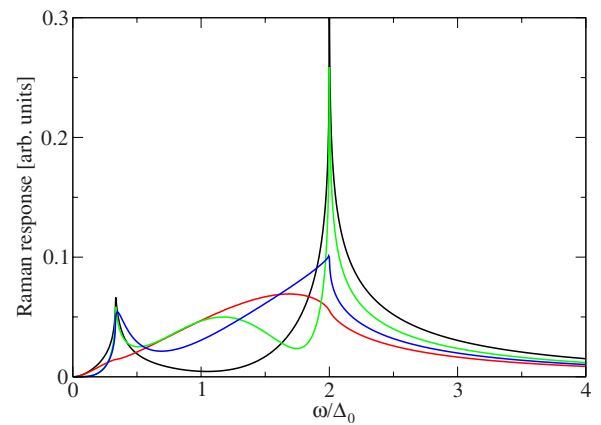

FIG. 3. (Color online) Raman response of the state with energy gap Eq. (10) for $r=1.4$. Black/gray (black/red) lines denote B_{1g}/B_{2g} and light gray/dark gray (green/blue) is the unscreened/screened A_{1g}, respectively. Note that our symmetry classifications are according to the geometry shown in Fig. 1. For lattice classifications, B_{1g} and B_{2g} should be interchanged.
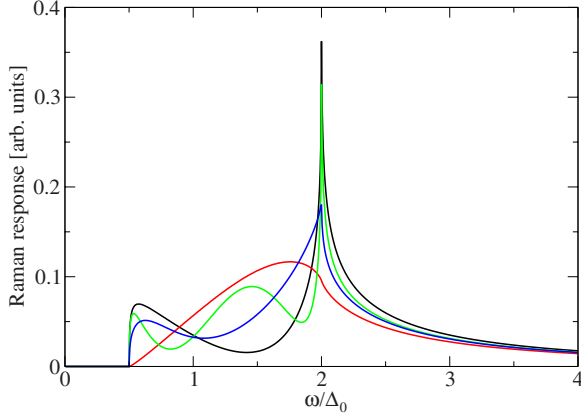
FIG. 4. (Color online) The Raman response of the state with energy gap Eq. (10) for $r=0.6$. Black/gray (black/red) lines denote B_{1g}/B_{2g}, respectively, light gray/dark gray (green/blue) is unscreened/screened A_{1g}.

2. Two Fermi-surface sheets

As indicated by Eq. (4), the A_{1g} Raman response for the case of a multisheet Fermi surface is not in general additive due to the Coulomb interactions and associated charge backflow. While no such backflow appears in the B_{1g} or B_{2g} channels for the present case, we will see in Sec. III that for Raman vertices which are allowed for the Fe pnictides, there can be Coulomb backflow contributions to the B_{1g} channel. To illustrate this we calculate the A_{1g} Raman response for two Fermi-surface sheets, where the energy gaps $\Delta_{1,2}(\Theta)$ are both proportional to $[1+r\cos(4\theta)]/(1+r)$, with $r=0.2$. For simplicity, we take the gap maximum on one Fermi surface to be Δ_0 and on the other $\Delta_0/2$. We also take equal Raman vertices and density of states for each band.

Expanding Eqs. (4)–(9) for the case of two bands, the overall Raman response can be written as

$$\text{Im } \chi_{sc}(\omega) = \text{Im } \chi_1(\omega) + \text{Im } \chi_2(\omega) + \text{Im } \Delta\chi(\omega), \quad (11)$$

where

$$\chi_{1,2}(\omega) = \frac{1}{N}\sum_{\mathbf{k}} \gamma_{1,2}^2(\mathbf{k})\lambda_{1,2}(\mathbf{k},\omega) - \frac{\left[\sum_{\mathbf{k}} \gamma_{1,2}(\mathbf{k})\lambda_{1,2}(\mathbf{k},\omega)\right]^2}{N\sum_{\mathbf{k}}\lambda_{1,2}(\mathbf{k},\omega)} \quad (12)$$

and

$$\Delta\chi(\omega) = \frac{\sum_{\mathbf{k}}\lambda_1(\mathbf{k},\omega)\sum_{\mathbf{k}}\lambda_2(\mathbf{k},\omega)}{N\sum_{\mathbf{k}}[\lambda_1(\mathbf{k},\omega) + \lambda_2(\mathbf{k},\omega)]}\left[\frac{\sum_{\mathbf{k}}\gamma_1(\mathbf{k})\lambda_1(\mathbf{k},\omega)}{\sum_{\mathbf{k}}\lambda_1(\mathbf{k},\omega)} - \frac{\sum_{\mathbf{k}}\gamma_2(\mathbf{k})\lambda_2(\mathbf{k},\omega)}{\sum_{\mathbf{k}}\lambda_2(\mathbf{k},\omega)}\right]^2. \quad (13)$$

Thus for A_{1g}, the screened Raman response can be considered as a sum of the screened response for each band, plus a mixing term $\Delta\chi$. Here one can see that if the energy gaps and Raman vertices are the same for each band the mixing term vanishes, while for all other cases it is finite, reflecting the
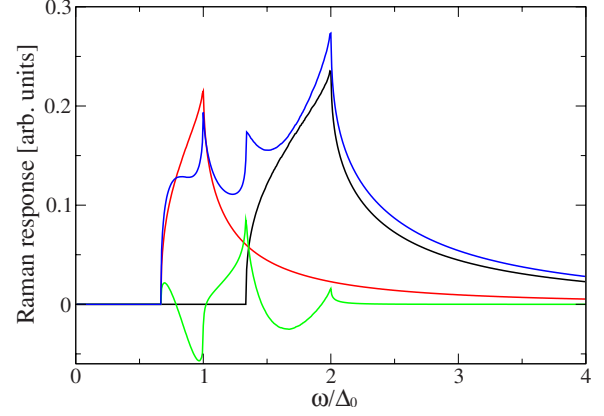

FIG. 5. (Color online) The screened A_{1g} Raman response for two bands with $\Delta_{1,2}(\theta)$ proportional to $[1+r\cos(4\theta)]/(1+r)$ with $r=0.2$ and the maximum gap on Fermi surface 1 equal to Δ_0 and on Fermi surface 2 equal to $\Delta_0/2$. (black=screened A_{1g} for band 1, gray (red)=screened A_{1g} for band 2, light gray (green)=mixing term, dark gray (blue)=total response).

contribution from charge backflow. In this case, the light scattering induces interband charge transfer in order to recover particle number conservation when the charge fluctuations differ on the two bands.

As illustrated in Fig. 5, the screened A_{1g} Raman spectrum consists of contributions from each Fermi surface with a gap scale differing by a factor of 2 and an interference contribution coming from the charge backflow. All singularities associated with the values of the gaps at the stationary points that would appear in the unscreened A_{1g} channel are removed and replaced by cusplike behavior as in the single band case. However the structure of $\chi_{sc}''(\omega)$ is changed by the interference.

Interference terms also occur if the gaps are identical on each sheet but the Raman vertices differ. A more detailed examination of the role of charge backflow is presented in Ref. 27.

III. FOUR FERMI-SURFACE RAMAN SPECTRA

We would now like to extend this discussion of the features in the Raman intensity to the four-Fermi surface model of the Fe pnictides. Here we first consider the two sets of $\Delta_\nu(\theta)$ gap variations for the four Fermi-surface sheets $\nu = \alpha_1, \alpha_2, \beta_1,$ and β_2 shown in Fig. 4. Specifically, the energy gaps are taken to be (Fig. 2)

$$\Delta_{\beta_1,\beta_2} = \Delta_0\frac{1\mp r_\beta \cos(2\theta)}{1+r_\beta},$$

$$\Delta_{\alpha_1} = -0.8\Delta_0\frac{1+\cos(4\theta)}{2},$$

$$\Delta_{\alpha_2} = -0.4\Delta_0\frac{1-\cos(4\theta)}{2}. \quad (14)$$

As previously discussed, these gap choices are motivated by the anisotropic gaps found in RPA spin fluctuation and func-

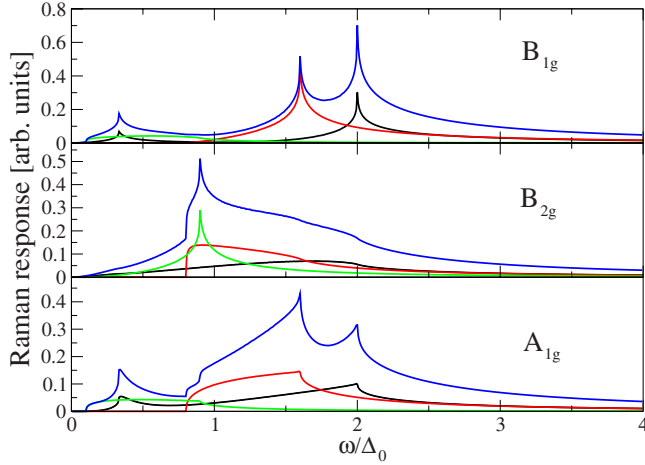FIG. 6. (Color online) The B_{1g}, B_{2g} and screened A_{1g} Raman spectra for a four-sheeted Fermi surface, with $r_\beta = 1.4$. Black line corresponds to each contribution from the $\beta_{1,2}$ bands, gray (red) line to the α_1 band, light gray (green) line to the α_2, and dark gray (blue) line is the total response. Note that for the A_{1g} case (bottom panel) there is an interference term in addition to the sum of the contributions from each band. The energy gaps used are defined in the text.

tional renormalization-group calculations. The amplitudes of the α_1 and α_2 gaps have been chosen to avoid an accidental overlap of singularities between the α and β gap extrema. The first of these, shown by the solid curves in Fig. 2, corresponds to an A_{1g} gap with nodes on the β-Fermi surfaces ($r_\beta = 1.4$) and the second one is nodeless corresponding to the dashed curves ($r_\beta = 0.6$). The B_{1g}, B_{2g}, and A_{1g} spectra for these two cases are shown in Figs. 6 and 7, respectively. The contribution from the individual Fermi surfaces are also indicated.

For the B_{1g} and B_{2g} spectra the structures seen in the total response are just the sum of the spectra from the individual Fermi-surface sheets with the appropriate gaps shown in Fig. 2. For example, in Fig. 6, the B_{1g} response for the gap with nodes consists of a sum over different contributions coming from the two hole Fermi surfaces α_1 and α_2 and the sum of the spectra from the β_1 and β_2 electron Fermi-surface sheets
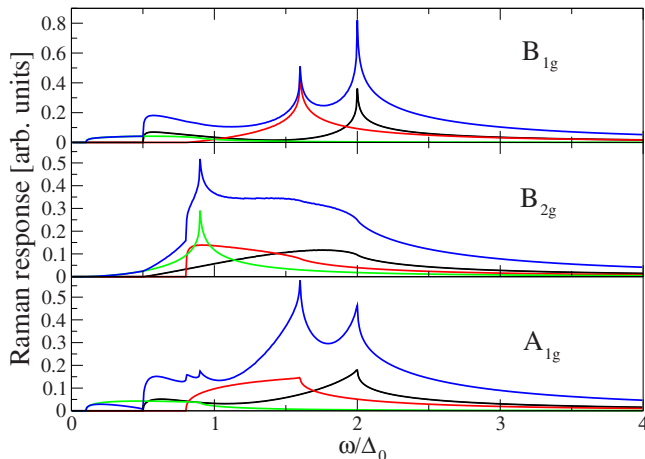

FIG. 7. (Color online) Same as Fig. 6 but for $r_\beta = 0.6$.

which are identical since Raman only probes $|\Delta|$ and is not sensitive to the phase in the absence of impurities. Just as the for the previous discussion of the single Fermi-surface case, one can easily identify the characteristic features coming from each Fermi surface shown in Fig. 6. The B_{1g} Raman response for a gap with nodes on the β sheets (red/gray curve) exhibits log singularities at ω/Δ_0 equal to $2\Delta_{\beta,\max}/\Delta_0 \simeq 1.5$ and $2|\Delta_\beta|_{\min}/\Delta_0 \simeq 0.25$. The α_1 sheet (green/light gray) contributes an additional log singularity at $2|\Delta_{\alpha_1}|_{\max}/\Delta_0 \simeq 1.6$. Since the B_{1g} vertex has a node at the minimum value of the gap on the α_1 sheet the discontinuity at $\omega/\Delta_0 = 0.8$ is eliminated leaving only a linear onset. The contribution of the α_2 sheet has a similar linear onset at $\omega = 0$ and a change in the slope at $2|\Delta_{\alpha_2}|_{\max}/\Delta_0 \simeq 0.8$ due to the fact that the B_{1g} Raman vertex has a node at the minimum and maximum values of the gap on the α_2 Fermi surface.

A similar discussion can be given for the B_{2g} case shown in the center panel of Fig. 6, where the total response is the sum of the contribution from the individual Fermi-surface sheets with the B_{2g} Raman vertex. As discussed in the previous section, the screened A_{1g} response shown in the lower panel of Fig. 6 contains the screened contributions from each band, plus an interference term with interference contributions coming from each pair of bands. All singularities are removed by the backflow, leaving the cusplike behavior which can be tied to each of the gap extrema, as done for the other channels.

As mentioned in Sec. II A, different forms for the Raman vertices are in principle allowable other than the ones given in Eq. (3), giving the Raman spectra shown in Figs. 6 and 7. Here we consider how different forms for the Raman vertices affect the general structure of the channel-dependent Raman spectra. As an example, we consider the following form for the Raman vertices:

$$\gamma_{\alpha_1,\alpha_2}(\theta)^{A_{1g}} = 1,$$

$$\gamma_{\beta_1,\beta_2}(\theta)^{A_{1g}} = -1,$$

$$\gamma_{\alpha_1,\alpha_2}(\theta)^{B_{1g}} = \cos(2\theta),$$

$$\gamma_{\beta_1,\beta_2}(\theta)^{B_{1g}} = \pm 1,$$

$$\gamma_{\alpha_1,\alpha_2}(\theta)^{B_{2g}} = \sin(2\theta),$$

$$\gamma_{\beta_1,\beta_2}(\theta)^{B_{2g}} = \sin(\theta). \tag{15}$$

These vertices are all allowed by symmetry and have less anisotropy than the ones considered in Eq. (3) and thus highlight different gap structures. Moreover, due to the angle-independent form for the B_{1g} vertices on the β sheets, screening must be included and the mixing terms are nonzero to give finite contributions to the spectra.

The resulting channel-dependent spectra are shown in Fig. 8 for the Fermi sheet gaps given in Eq. (14) with $r_\beta = 1.4$. For the B_{1g} case, Raman scattering from the individual β sheets now is canceled by backflow due to the angular-independent Raman vertices on those sheets and two identical contribu-
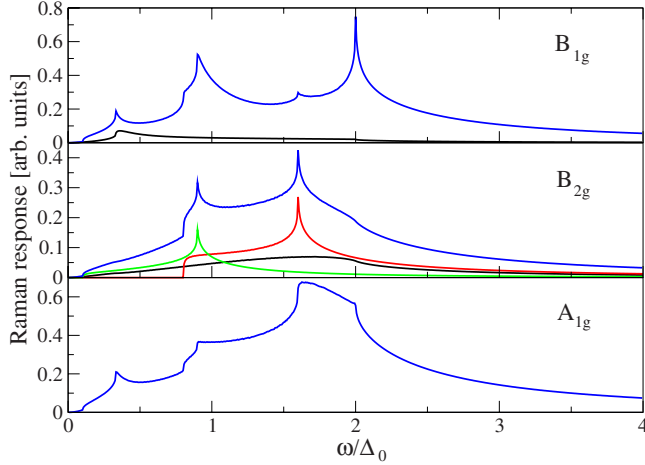
FIG. 8. (Color online) Same as Fig. 6 but for different Raman vertices, given by Eq. (15).

FIG. 9. (Color online) Polarization dependence Raman response for the $s\pm$ state, having energy gaps given by Eq. (16) and Raman vertices given by Eq. (15). Color scales, denoting contributions from each band and the total response, are the same as in Figs. 6–8.

tions arise from the α sheets, as in Fig. 6. However, an additional mixing term arising from scattering interferences involving each separate β sheet gives a large contribution to the spectra, with peaks occurring at the energy scales given by the energy-gap extrema on each sheet. For the B_{2g} spectra, the sinusoidal variation $\sin(\theta)$ of the vertices on the β sheets now allows for the highlighting of the gap maximum, giving a peak frequency at twice the gap maximum for the β sheets, in contrast to the spectra shown in Fig. 6. A dramatic change of the spectra is observed for the A_{1g} channel. Due to backflow, the Raman response from each separate band vanishes identically for the constant vertices in Eq. (15), but due to the change in sign, the entire Raman spectra arise solely from the mixing. The positions of the cusplike feature at $\omega = 2\Delta_0$ are the same as that shown in Fig. 6 for a different form for the Raman vertices, however the overall spectra line shape is qualitatively different. The overall structure of the line shapes thus indicates that a proper account of the anisotropy of the Raman vertices may be needed in order to obtain a qualitative comparison to the experimental observed Raman spectra. This is a topic for further study.

Finally we consider a simple sign-changing $s\pm$ state on the four sheets

$$\Delta_{\beta_1,\beta_2} = -\Delta_0/\sqrt{2},$$

$$\Delta_{\alpha_1} = \Delta_0, \quad \Delta_{\alpha_2} = \Delta_0/4. \quad (16)$$

Using the vertices defined by Eq. (15), the resulting Raman spectra are shown in Fig. 9. Here, the square-root divergence at twice the gap value is ubiquitous, displaying both in B_{1g} and in B_{2g} The only polarization difference is that the contributions from the β bands for the B_{1g} channel are screened, in contrast to the B_{1g} channel. Apart from this difference, the spectra are qualitatively similar due to the mixing terms in B_{1g} which restore the singularity at $\omega = 1.5\Delta_0$. For the A_{1g} channel, the divergences are screened and the response maintains thresholds and peaks at twice the gap energy for each band.
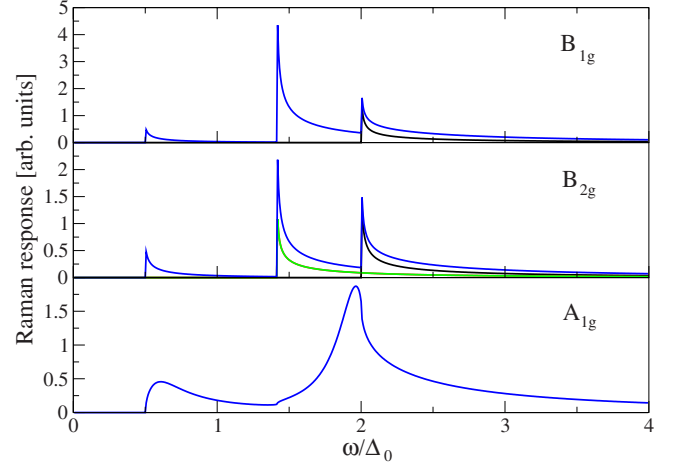
IV. CONCLUSIONS

Here we have studied the Raman-scattering response for some simple models of the Fe-pnictide superconductors. Specifically, we considered two different anisotropic A_{1g} gaps, one with nodes and one without nodes, on four circular Fermi surfaces. Besides the well-known low-frequency differences in the spectra for nodal and non-nodal gaps, we found a rich set of high-frequency structures arising from stationary points of $\Delta_\nu(\theta)$ on the various Fermi-surface sheets. Measurements of different polarizations may allow one to associate particular gap structures with individual Fermi-surface sheets. If the gap has a large anisotropy as suggested by some calculations, there will be a rich Raman spectrum for different symmetry channels. However, if one has a relatively isotropic gap, such as the proposed sign-switched s wave, the spectrum should be simpler and sharper since for an isotropic gap the response has a square-root singularity at $2\Delta_0$ rather than the weaker log singularity found for an anisotropic gap.

We have also discussed some of the unusual aspects of the Raman spectra to be anticipated in the Fe pnictides due to their multisheeted Fermi-surface electronic structure. In particular, Coulomb backflow mixing may affect the B_{1g} spectrum as well as A_{1g}. There are other unusual aspects, such as excitonic modes associated with short-range interactions[38] or competing order-parameter channels, which we have not explored here, but may make the spectra in these materials even richer. Work along these lines is in progress.

Note added in proof. Neutron scattering measurements of doped BaFe$_2$As$_2$ find a resonance in the superconducting state which through the coherence factor provides phase sensitive evidence of an unconventional gap.[39]

ACKNOWLEDGMENTS

[1] Y. Kamihara, T. Watanabe, M. Hirano, and H. Hosono, J. Am. Chem. Soc. **130**, 3296 (2008).

[2] M. V. Sadovskii, Physics Uspekhi, 51, 102 (2008).

[3] H. Aoki, arXiv:0811.1656 (unpublished).

[4] I. Mazin and J. Schmalian, arXiv:0901.4790 (unpublished).

[5] R. Klingeler, N. Leps, I. Hellmann, A. Popa, C. Hess, A. Kondrat, J. Hamann-Borrero, G. Behr, V. Kataev, and B. Buechner, arXiv:0808.0708 (unpublished).

[6] H.-J. Grafe, D. Paar, G. Lang, N. J. Curro, G. Behr, J. Werner, J. Hamann-Borrero, C. Hess, N. Leps, R. Klingeler, and B. Buchner, Phys. Rev. Lett. **101**, 047003 (2008).

[7] K. Ahilan, F. L. Ning, T. Imai, A. S. Sefat, R. Jin, M. A. McGuire, B. C. Sales, D. Mandrus, Phys. Rev. B **78**, 100501(R) (2008).

[8] T. Y. Nakai *et al.*, J. Phys. Soc. Jpn. **77**, 073701 (2008).

[9] K. Hashimoto, T. Shibauchi, T. Kato, K. Ikada, R. Okazaki, H. Shishido, M. Ishikado, H. Kito, A. Iyo, H. Eisaki, S. Shamoto, and Y. Matsuda, Phys. Rev. Lett. **102**, 017002 (2009).

[10] C. Martin, M. E. Tillman, H. Kim, M. A. Tanator, S. K. Kim, A. Kreyssig, R. T. Gordon, M. D. Vannette, S. Nandi, V. G. Kogan, S. L. Bud'ko, P. C. Canfield, A. I. Goldman, and R. Pozorov, arXiv:0903.2220 (unpublished).

[11] C. Martin, R. T. Gordon, M. A. Tanatar, M. D. Vannette, M. E. Tillman, E. D. Mun, P. C. Canfield, V. G. Kogan, G. D. Samolyuk, J. Schmalian, and R. Prozorov, arXiv:0903.2220 (unpublished).

[12] K. Hashimoto, I. Shibauchi, S. Kasahara, K. Ikada, T. Kato, R. Okazaki, C. Vanderbeek, M. Konczykowski, H. Takeya, K. Hirata, T. Terashima, and Y. Matsuda, arXiv:0810.3506 (unpublished).

[13] R. T. Gordon, N. Ni, C. Martin, M. A. Tanatar, M. D. Vannette, H. Kim, G. Samolyuk, J. Schmalian, S. Nandi, A. Kreyssig, A. I. Goldman, J. Q. Yan, S. L. Bud'ko, P. C. Canfield, and R. Prozorov, Phys. Rev. Lett. **102**, 127004 (2009).

[14] R. T. Gordon, C. Martin, H. Kim, N. Ni, M. A. Tanatar, J. Schmalian, I. I. Mazin, S. L. Bud'ko, P. C. Canfield, and R. Prozorov, Phys. Rev. B **79**, 100506(R) (2009).

[15] J. D. Fletcher, A. Serafin, L. Malone, J. Analytis, J.-H. Chu, A. S. Erickson, I. R. Fisher, and A. Carrington, arXiv:0812.3858 (unpublished).

[16] L. Zhao, H.-Y. Liu, W.-T. Zhang, J.-Q. Meng, X.-W. Jia, G.-D. Liu, X.-L. Dong, G.-F. Chen, J.-L. Luo, N.-L. Wang, W.-L. Lu, G.-L. Wang, Y. Zhou, Y. Zhu, X.-Y. Wang, Z.-Y. Xu, C.-T. Chen, and X.-J. Zhou, Chin. Phys. Lett. **25**, 4402 (2008).

[17] H. Ding, P. Richard, K. Nakayama, T. Sugawara, T. Arakane, Y. Sekiba, A. Takayama, S. Souma, T. Sato, T. Takahashi, Z. Wang, X. Dai, Z. Fang, G. F. Chen, J. L. Luo, and N. L. Wang, Europhys. Lett. **83**, 47001 (2008).

[18] T. Kondo, A. F. Santander-Syro, O. Copie, C. Liu, M. E. Tillman, E. D. Mun, J. Schmalian, S. L. Bud'ko, M. A. Tanatar, P. C. Canfield, and A. Kaminski, Phys. Rev. Lett. **101**, 147003 (2008).

[19] D. V. Evtushinsky, D. S. Inosov, V. B. Zabolotnyy, A. Koitzsch, M. Knupfer, B. Buchner, G. L. Sun, V. Hinkov, A. V. Boris, C. T. Lin, B. Keimer, A. Varykhalov, A. A. Kordyuk, and S. V. Borisenko, Phys. Rev. B **79**, 054517 (2009).

[20] K. Nakayama, T. Sato, P. Richard, Y.-M. Xu, Y. Sekiba, S. Souma, G. F. Chen, J. L. Luo, N. L. Wang, H. Ding, and T. Takahashi, EPL **85**, 67002 (2009).

[21] L. Wray, D. Qian, D. Hsieh, Y. Xia, L. Li, J. G. Checkelsky, A. Pasupathy, K. K. Gomes, C. V. Parker, A. V. Fedorov, G. F. Chen, J. L. Luo, A. Yazdani, N. P. Ong, N. L. Wang, and M. Z. Hasan, Phys. Rev. B **78**, 184508 (2008).

[22] A. B. Vorontsov, M. G. Vavilov, and A. V. Chubukov, arXiv:0901.0719 (unpublished).

[23] V. Mishra, G. Boyd, S. Graser, T. Maier, P. J. Hirschfeld, and D. J. Scalapino, Phys. Rev. B **79**, 094512 (2009).

[24] T. P. Devereaux and R. Hackl, Rev. Mod. Phys. **79**, 175 (2007).

[25] T. P. Devereaux and A. Kampf, Int. J. Mod. Phys. B **11**, 2093 (1995).

[26] T. P. Devereaux and D. Einzel, Phys. Rev. B **51**, 16336 (1995).

[27] T. P. Devereaux, A. Virosztek, and A. Zawadowski, Phys. Rev. B **54**, 12523 (1996).

[28] D. J. Singh and M.-H. Du, Phys. Rev. Lett. **100**, 237003 (2008).

[29] C. Cao, P. J. Hirschfeld, and H.-P. Cheng, Phys. Rev. B **77**, 220506(R) (2008).

[30] K. Kuroki, S. Onari, R. Arita, H. Usui, Y. Tanaka, H. Kontani, and H. Aoki, Phys. Rev. Lett. **101**, 087004 (2008).

[31] H. Ikeda, J. Phys. Soc. Jpn. **77**, 123707 (2008).

[32] Y. Yanagi, Y. Yamakawa, and Y. Ono, J. Phys. Soc. Jpn. **77**, 123701 (2008).

[33] S. Graser, T. A. Maier, P. J. Hirschfeld, and D. J. Scalapino, New J. Phys. **11**, 025016 (2009).

[34] F. Wang, H. Zhai, Y. Ran, A. Vishwanath, and D.-H. Lee, Phys. Rev. Lett.. **102**, 047005 (2009).

[35] I. I. Mazin, D. J. Singh, M. D. Johannes, and M. H. Du, Phys. Rev. Lett. **101**, 057003 (2008).

[36] A. V. Chubukov, D. V. Efremov, and I. Eremin, Phys. Rev. B **78**, 134512 (2008).

[37] S. Graser, G. R. Boyd, C. Cao, H. P. Cheng, P. J. Hirschfeld, and D. J. Scalapino, Phys. Rev. B **77**, 180514(R) (2008).

[38] A. V. Chubukov, I. Eremin, and M. M. Korshunov, arXiv:0901.2102 (unpublished).

[39] A. D. Christianson, E. A. Goremychkin, R. Osborn, S. Rosenkranz, M. D. Lumsden, C. D. Malliakas, L. S. Todorov, H. Claus, D. Y. Chung, M. G. Kantazidis, R. I. Bewley, and T. Guidi, Nature **456**, 930 (2008).